



This is a repository copy of *Feature-refined box particle filtering for autonomous vehicle localisation with OpenStreetMap*.

White Rose Research Online URL for this paper:
<https://eprints.whiterose.ac.uk/177243/>

Version: Accepted Version

Article:

Wang, P., Mihaylova, L. orcid.org/0000-0001-5856-2223, Bonnifait, P. et al. (2 more authors) (2021) Feature-refined box particle filtering for autonomous vehicle localisation with OpenStreetMap. *Engineering Applications of Artificial Intelligence*, 105. 104445. ISSN 0952-1976

<https://doi.org/10.1016/j.engappai.2021.104445>

Article available under the terms of the CC-BY-NC-ND licence (<https://creativecommons.org/licenses/by-nc-nd/4.0/>).

Reuse

This article is distributed under the terms of the Creative Commons Attribution-NonCommercial-NoDerivs (CC BY-NC-ND) licence. This licence only allows you to download this work and share it with others as long as you credit the authors, but you can't change the article in any way or use it commercially. More information and the full terms of the licence here: <https://creativecommons.org/licenses/>

Takedown

If you consider content in White Rose Research Online to be in breach of UK law, please notify us by emailing eprints@whiterose.ac.uk including the URL of the record and the reason for the withdrawal request.



eprints@whiterose.ac.uk
<https://eprints.whiterose.ac.uk/>

Feature-refined Box Particle Filtering for Autonomous Vehicle Localisation with OpenStreetMap

Peng Wang^{a,*}, Lyudmila Mihaylova^a, Philippe Bonnifait^b, Philippe Xu^b,
Jianwen Jiang^c

^a*Dept. of Automatic Control and Systems Engineering, The University of Sheffield,
Sheffield S10 3JD, United Kingdom*

^b*Université de Technologie de Compiègne, CNRS, Heudiasyc, 60 203 Compiègne, France*

^c*Dept. of Automation, University of Science and Technology of China, Hefei, 230027,
P.R.China*

Abstract

Vehicle localisation is an important and challenging task in achieving autonomous driving. This work presents a box particle filter framework for vehicle self-localisation in the presence of sensor and map uncertainties. The proposed feature-refined box particle filter incorporates line features extracted from a multi-layer Light Detection And Ranging (LiDAR) sensor and information from OpenStreetMap to estimate the vehicle state. A particle weight balance strategy is incorporated to account for the OpenStreetMap inaccuracy, which is assessed by comparing it to a high definition road map. The performance of the proposed framework is evaluated on a LiDAR dataset and compared with box particle filter variants. Experimental results show that the proposed framework achieves respectively 10% and 53% localisation accuracy improvement with reduced box volumes of 25% and 41%, when compared with the state-of-the-art interval analysis based box regularisation particle filter and the box particle filter.

Keywords: Localisation, Box particle filtering, Autonomous vehicles, Information uncertainty, OpenStreetMap

*Corresponding author

Email addresses: Peng.Wang@Sheffield.ac.uk (Peng Wang),
l.s.mihaylova@Sheffield.ac.uk (Lyudmila Mihaylova), philippe.bonnifait@hds.utc.fr
(Philippe Bonnifait), philippe.xu@hds.utc.fr (Philippe Xu), jjwen@mail.ustc.edu.cn
(Jianwen Jiang)

1. Introduction

The development of reliable autonomous driving solutions is an active research area (Pendleton et al., 2017, Reid et al., 2019). Localisation plays a key role of autonomous systems since it provides the vehicle with self-awareness of its state $\mathbf{x}_k = (x_k, y_k, \theta_k)^T$, which encodes its position (x_k, y_k) and its orientation θ_k relative to a map (Kuutti et al., 2018) at time k .

There are mainly two main types of maps used for localising a vehicle: (1) maps that are incrementally built and maintained along with localisation; (2) accurate commercial digital maps that are built and maintained by companies. *Feature maps* (Holý, 2018) and *point-cloud maps* (Javanmardi et al., 2019, Tamas and Goron, 2014) belong to the first group. In general, feature maps represent the environment with geometrical features at various levels; whereas point-cloud maps are usually built by registering point clouds to a geographic information system (Zhang and Singh, 2014). The former is known for its semantic interpretability and low complexity, while the latter is computational resources dependant and holds the promise of high accuracy. These two types of maps are generally components of simultaneous localisation and mapping (SLAM) solutions (Gil et al., 2015, Li et al., 2019). Therefore, they inherit the challenges faced by SLAM approaches, such as localisation accuracy degradation when the uncertainty of sensor measurements increases. In such cases, loop closure and subsequent optimisation techniques are widely adopted to respectively improve the mapping accuracy (Wang et al., 2016) and the localisation results. However, a unified SLAM framework for mapping and maintaining high accuracy is still difficult, causing the inaccuracy of the obtained maps.

The second group of accurate digital maps comes with service charges and often limited access to metadata. The crowdsourced OpenStreetMap (OSM) could be a cheaper replacement for expensive digital maps and can provide flexible solutions since almost all the metadata can be accessed and customised by end-users. OSM has already been applied in urban navigation (Suger and Burgard, 2017). However, the accuracy of OSM remains a challenge (Vargas-

31 [Munoz et al., 2021](#)). It could vary from centimeters to meters from city to
32 city, thus bringing in additional uncertainties apart from those caused by sen-
33 sors ([Brovelli et al., 2016](#), [Senaratne et al., 2017](#)). Hence, it is beneficial to
34 develop robust localisation frameworks when using inaccurate SLAM maps or
35 OSM for autonomous systems.

36 In this paper, a feature-refined BPF (FRBPF) that stems from the box
37 particle filtering (BPF) approach ([Abdallah et al., 2008](#), [Gning et al., 2013](#))
38 is proposed to achieve accurate and robust localisation results based on an
39 inaccurate yet free OSM. In our case, the OSM serves as a reference map for
40 localising a vehicle. A real-time kinematic (RTK) sensor suite provides the
41 ground truth information. The vehicle is equipped with an Inertial Measurement
42 Unit (IMU) and a LiDAR sensor to fulfill localisation.

43 In the proposed approach, line features are firstly extracted from raw LiDAR
44 data obtained by the vehicle at time k . The distances and angles of the line fea-
45 tures with respect to the vehicle are adopted as measurements and are denoted
46 as $[\mathbf{y}_k]$. The line features are next associated with line features correspond-
47 ing to building footprints on the OSM. The accuracy of the OSM is assessed
48 with respect to a high-definition map (HDM) maintained by the Université de
49 Technologie de Compiègne (UTC) so that map uncertainties are also considered
50 during localisation. Measurements of the matched line features are fed to the
51 proposed FRBPF for vehicle state updating. With N box particles representing
52 the vehicle states $[\mathbf{x}_k^i]$, $i = 1, \dots, N$ and upon the arrival of measurements $[\mathbf{y}_k]$,
53 the filter propagates state estimates through the box contraction and update
54 steps as time evolves. In contrast of performing contraction per measurement,
55 a feature-refined contraction merges line features before the contraction step.
56 This is also a way of coping with OSM and sensor data uncertainties, hence-
57 forth reduces boxes. As interval analysis based methods do not provide point
58 estimates by nature, this paper takes box centers to achieve point estimates by
59 statistical metrics such as expectation and covariance to evaluate the proposed
60 FRBPF and compares it with the BPF and the box regularised particle filter
61 (BRPF) ([Merlinge et al., 2019](#)).

62 The main contributions of this paper can be summarised as follows: (1) A
63 LiDAR features-refined box particle filter is proposed that is able to deal effec-
64 tively with OSM and sensor data uncertainties; (2) A contraction algorithm is
65 developed that incorporates the abundant line features from structured urban
66 environments to reduce the volume of box particles; (3) Theoretical proofs about
67 the features-refined contractions are derived; (4) A box particle weight balance
68 strategy is designed to cope with OSM uncertainties and further improves the
69 localisation performance.

70 The rest of this paper is organised as follows. Section 2 presents an overview
71 of related works. Section 3 gives the necessary theoretical background knowl-
72 edge. Section 4 elaborates the proposed approach. Section 5 includes valida-
73 tion and discussions of the proposed approach. Finally, conclusions and future
74 works are given in Section 6. Appendix A and Appendix B prove that the
75 feature-refined contraction reduces the particle box volume compared with the
76 traditional contraction.

77 2. Related Works

78 2.1. OpenStreetMap based Localisation

79 OSM is the most well-known crowdsourced map whose metadata is struc-
80 tured by entities such as *nodes*, *ways*, and *relations* (Zheng and Izzat, 2018).
81 *Nodes* represent points of interest. *Ways* are a collection of *nodes* that corre-
82 spond to buildings and roads, and *relations* indicate the relationships between
83 *nodes* and *ways*. Generally, the exterior surface of buildings can be projected
84 into a two dimensional (2D) plane as line segments or can be approximated by
85 line segments. Hence, the OSM is equivalent to a feature map represented by a
86 set of linear equations.

87 Compared with highly precise maps, maintained by local authorities, the
88 OSM accuracy needs to be further improved. For instance, building footprints
89 of Milan on OSM show a systematic translation of 0.4 m on the defined X
90 and Y directions in (Brovelli et al., 2016). Furthermore, applications of OSM

91 still suffer from the incompleteness of buildings, roads and other environmental
92 factors (Senaratne et al., 2017).

93 Nevertheless, OSM has been widely used in vehicle/robot localisation. Suger
94 and Burgard (Suger and Burgard, 2017) present a Markov Chain Monte Carlo
95 approach for autonomous robot navigation, by associating track information
96 from OSM with trails detected by the robot based on three dimensional (3D)
97 LiDAR data. The robustness of the approach is demonstrated with experimental
98 results, which shows the potential of using inaccurate OSM in urban environ-
99 ments. Zheng and Izzat (Zheng and Izzat, 2018) show that by taking OSM as
100 a prior map, one can benefit from road perception by first rendering a virtual
101 street view, and further refining it to provide prior road masks. The road mask
102 can be augmented into drivable space by integrating images or LiDAR point
103 clouds. By taking the road mask as image inputs to a fully convolutional neural
104 network, the authors also discuss the promise of deep learning methods com-
105 bined with OSM for road perception. Joshi and James (Joshi and James, 2015)
106 propose to combine coarse, inaccurate prior maps from OSM with local sensor
107 information from 3D LiDAR to localise a vehicle. Lane locations are estimated
108 by particle filter variants and then integrated within a map to further improve
109 the localisation accuracy.

110 *2.2. Box Particle Filtering based Localisation*

111 Recently, interval analysis based localisation has shown its potential in deal-
112 ing with non-Gaussian and biased noise perturbed measurements. The combina-
113 tion of the set-membership framework with particle filtering techniques known
114 as BPF is first introduced by Abdallah et al (Abdallah et al., 2008) to localise
115 a ground vehicle. The application of the BPF to global localisation shows that
116 with only 10 box particles, BPF reaches almost the same accuracy as particle
117 filter with 3,000 particles.

118 Ever since then, BPF has been applied to different scenarios. Gning et
119 al. (Gning et al., 2012) introduced the Bernoulli BPF and applied it to tracking
120 a single target. It shows that the Bernoulli BPF can track the target accurately

121 and is computationally more efficient compared with the Bernoulli particle filter.
 122 A multiple extended object tracking method based on BPF is further proposed
 123 by Freitas et al. (Freitas et al., 2018), which benefits from the fact that BPF
 124 can well tackle ambiguous observations, which often happens in LiDAR and
 125 GPS data. Merlinge et al. (Merlinge et al., 2019) propose the BRPF that
 126 outperforms the BPF in terms of Root Mean Square Errors (RMSEs). The
 127 BRPF achieves up to 42% improvement in geographical position estimation
 128 compared with BPF. The authors also demonstrate that both BRPF and BPF
 129 produce lower divergence rate ($\leq 1\%$) than methods such as particle filters.
 130 Luo et al. (Luo and Qin, 2018) propose the ball particle filter to deal with
 131 issues caused by box subdivision and forward-backward contraction. In the
 132 ball particle filter, boxes in BPF are replaced by balls, and a ball contractor is
 133 proposed to contract the balls. Applications of the ball particle filter in SLAM
 134 show that with 20 particles, the ball particle filter achieves 34.5% and 34.6%
 135 position and orientation improvement, respectively. However, the results show
 136 that the ball particle filter is about 7% less efficient than the BPF. Nevertheless,
 137 all the methods perform contraction when a measurement is obtained, without
 138 further integration or refinement. Furthermore, the BPF has not been applied
 139 to OSM based localisation.

140 3. Theoretical Background

141 3.1. Boxes and Inclusion Functions

In interval analysis, intervals or boxes are used as basic operands for mod-
 elling and calculation, etc. An interval or box is defined as

$$[\mathbf{x}] = ([x_1], \dots, [x_i], \dots, [x_d])^T \in \mathbb{IR}^d,$$

142 where $[x_i] = [\underline{x}_i, \bar{x}_i]$ with $\underline{x}_i, \bar{x}_i \in \mathbb{R}$, and $\forall x_i \in [x_i], \underline{x}_i \leq x_i \leq \bar{x}_i$ stands.
 143 \mathbb{IR}^d and \mathbb{R} are respectively the $d \in \mathbb{N}^+$ dimensional real interval space and the
 144 real number space (Alefeld and Mayer, 2000). When $[\mathbf{x}]$ is one dimensional,
 145 it is usually called an interval, and it is called a box when the dimension is

146 two or above. This paper adopts ‘box’ to refer to both intervals and boxes
 147 hereafter for brevity. The volume of a box is defined as $|\mathbf{x}| = \prod_{i=1}^d |[x_i]|$,
 148 where $|[x_i]| = \bar{x}_i - \underline{x}_i$ (Ilog, 1999). Note when $d = 1$, ‘volume’ refers to the size
 149 of the one dimensional interval, and when $d = 2$, it refers to the area of the two
 150 dimensional box. For brevity and generality, this paper uses ‘volume’ to refer
 151 to all the scenarios, unless otherwise specified.

152 Given boxes \mathbf{x} , \mathbf{y} , and an operator $\diamond \in \{+, -, \dots, /\}$, $\mathbf{x} \diamond \mathbf{y}$ is defined as
 153 the smallest box in terms of volume that contains all feasible values of $\mathbf{x} \diamond \mathbf{y}$. For
 154 a given box \mathbf{x} , its center is defined as $\mathbf{c}_\mathbf{x} = ((\underline{x}_1 + \bar{x}_1)/2, \dots, (\underline{x}_d + \bar{x}_d)/2)^T$ (Drev-
 155 elle and Bonnifait, 2013).

156 In general, when applying a function $\mathbf{f} : \mathbb{R}^{d_1} \rightarrow \mathbb{R}^{d_2}$ ($d_1, d_2 \in \mathbb{N}^+$) that is
 157 defined in the real number space directly to manipulate a box \mathbf{x} , one cannot
 158 guarantee that $\mathbf{f}(\mathbf{x})$ is still a box. In interval analysis, the inclusion function
 159 $[\mathbf{f}]$ is taken as a counterpart of \mathbf{f} to ensure that $[\mathbf{f}](\mathbf{x})$ is still a box. The
 160 inclusion function is normally defined as $\mathbf{f}(\mathbf{x}) \subset [\mathbf{f}](\mathbf{x})$, $\forall \mathbf{x} \subset \mathbb{I}\mathbb{R}^d$ (Jaulin
 161 and Desrochers, 2014, Jaulin et al., 2001).

162 3.2. Constraint Satisfaction Problems

163 When a box propagates through an inclusion function, its volume could
 164 increase dramatically. This reveals the ‘conservative’ nature of interval analy-
 165 sis based methods, i.e. expanding box volumes to guarantee that no feasible
 166 solutions are excluded. This, however, can cause overestimation problems as
 167 non-feasible solutions could be included as well when a box is expanded. The
 168 Constraint Satisfaction Problem (CSP) is exploited to help reducing box vol-
 169 umes. The CSP aims at finding a subset X of the feasible domain \mathbf{x} , which
 170 satisfies

$$X = \{\mathbf{x} \in \mathbf{x} \mid \mathbf{h}(\mathbf{x}) = 0\}, \quad (1)$$

171 where $\mathbf{h}(\mathbf{x}) = 0$ indicates the constraint. Finding X is computationally demand-
 172 ing. In interval analysis, instead of finding X , one can apply a contractor \mathcal{C} to
 173 reduce the volume of \mathbf{x} and get $\mathbf{x}_c = \mathcal{C}(\mathbf{x})$, such that $X \subset \mathbf{x}_c \subseteq \mathbf{x}$ (Drev-
 174 elle and Bonnifait, 2013).

175 The forward-backward contractor is broadly accepted in literature due to its
 176 efficiency and effectiveness. Given a set of constraints in the form of $\mathbf{h}(\mathbf{x}) =$
 177 \mathbf{y} , with \mathbf{x} and \mathbf{y} measurable quantities, the contraction is achieved (Jaulin,
 178 2009a) by propagating from \mathbf{x} to \mathbf{y} in the first step (*forward propagation*). The
 179 constraints are next propagated inversely from \mathbf{y} to \mathbf{x} (*backward propagation*).
 180 The process is repeated until no more significant box volume reduction can be
 181 observed. Jaulin gives some examples to make the process easy to understand
 182 in (Jaulin, 2009a).

183 3.3. The q -satisfied Intersection

184 For a given set of $Q \in \mathbb{N}^+$ boxes $\{[\mathbf{x}]_i, i = 1, \dots, Q\}$, the computation of
 185 their intersection

$$[\mathbf{x}] = \bigcap_{i=1}^Q [\mathbf{x}]_i \quad (2)$$

186 is frequently required. However, outliers cause empty intersections, which can
 187 lead to early termination or even divergence of algorithms.

188 The q -satisfied intersection (Wang et al., 2015, 2018) along with the q -relaxed
 189 intersection proposed in (Jaulin, 2009b) are used to find a subset of $\{[\mathbf{x}]_i, i =$
 190 $1, \dots, Q\}$, such that their intersection is not empty. The difference between
 191 the two is that the q -satisfied method searches for the maximum number q of
 192 boxes with non-empty intersection, where q is not determined at the beginning.
 193 While in the q -relaxed intersection, q is normally determined according to the
 194 application. In the q -satisfied intersection, q is defined as

$$q = \max \left\{ \text{card}(A) \mid A \subseteq \{1, \dots, Q\}, \bigcap_{j \in A} [\mathbf{x}]_j \neq \emptyset \right\}, \quad (3)$$

195 with $\text{card}(A)$ indicates the cardinality of set A . Subsequently a q -satisfied in-
 196 tersection is defined as

$$[\mathcal{A}_i] = \bigcap^{\{q\}} [\mathbf{x}]_{1, \dots, Q} = \bigcap_{j \in A} [\mathbf{x}]_j, \quad \text{card}(A) = q. \quad (4)$$

197 Usually, one can get $K \in \mathbb{N}^+$ q -satisfied intersections $[\mathcal{A}_1], \dots, [\mathcal{A}_K]$. An
 198 approximation to (2) is then denoted as

$$[\mathbf{x}] = \bigcap_{i=1}^Q [\mathbf{x}_i] = \mathcal{B}(\{[\mathcal{A}_1], \dots, [\mathcal{A}_K]\}), \quad (5)$$

199 where $\mathcal{B}(\cdot)$ indicates the minimum box that encloses $\{[\mathcal{A}_1], \dots, [\mathcal{A}_K]\}$.

200 In this paper, q is found by decreasing Q by 1 each step and check whether
 201 (3) is satisfied. In scenarios where real-time performance is critical, one can
 202 decreasing Q by a greater than 1 step to accelerate the process.

203 4. Feature Refined Box Particle Filter for Localisation

204 4.1. Problem Description

205 The motion of a vehicle is usually described by an evolution model \mathbf{f} and an
 206 observation model \mathbf{g} . The former represents dynamics of the vehicle, and the
 207 latter reveals what measurements the vehicle can incorporate to locate itself.
 208 They are separately represented as

$$\begin{cases} \mathbf{x}_k = \mathbf{f}(\mathbf{x}_{k-1}, \mathbf{u}_k) + \boldsymbol{\mu}_k, \\ \mathbf{y}_k = \mathbf{g}(\mathbf{x}_k, \mathbf{m}) + \boldsymbol{\nu}_k, \end{cases} \quad (6)$$

209 where \mathbf{x}_{k-1} and \mathbf{x}_k are vehicle states at $k-1$ and k , \mathbf{y}_k denotes the measurement,
 210 \mathbf{m} is the reference map, $\mathbf{u}_k = [v_k, \omega_k]^T$ is the input with v_k the vehicle speed and
 211 $\omega_k = \dot{\theta}_k$ the yaw rate, and $\boldsymbol{\mu}_k$ and $\boldsymbol{\nu}_k$ are separately the system and observation
 212 noises.

213 In the Bayesian framework, the objective of localising a vehicle is to estimate
 214 the posterior distribution over the current vehicle pose \mathbf{x}_k denoted as

$$\begin{aligned} & p(\mathbf{x}_k \mid \mathbf{y}_{1:k}, \mathbf{u}_{1:k}, \mathbf{m}) \\ &= \frac{1}{\chi_k} p(\mathbf{y}_k \mid \mathbf{x}_k, \mathbf{m}) p(\mathbf{x}_k \mid \mathbf{y}_{1:k-1}, \mathbf{u}_{1:k}, \mathbf{m}), \end{aligned} \quad (7)$$

215 where

$$216 \chi_k = \int p(\mathbf{y}_k \mid \mathbf{x}_k, \mathbf{m}) p(\mathbf{x}_k \mid \mathbf{y}_{1:k-1}, \mathbf{u}_{1:k}, \mathbf{m}) d\mathbf{x}_k$$

217 is the evidence distribution. Equation (7) can be decomposed into two compo-
 218 nents besides $\frac{1}{\chi_k}$. The predictive distribution is defined as

$$\begin{aligned} & p(\mathbf{x}_k \mid \mathbf{y}_{1:k-1}, \mathbf{u}_{1:k}, \mathbf{m}) \\ = & \int p(\mathbf{x}_k \mid \mathbf{x}_{k-1}, \mathbf{u}_k) p(\mathbf{x}_{k-1} \mid \mathbf{y}_{1:k-1}, \mathbf{u}_{1:k-1}, \mathbf{m}) d\mathbf{x}_{k-1}, \end{aligned} \quad (8)$$

219 where $p(\mathbf{x}_k \mid \mathbf{x}_{k-1}, \mathbf{u}_k)$ indicates the state transitional density, and the prior
 220 distribution $p(\mathbf{x}_{k-1} \mid \mathbf{y}_{1:k-1}, \mathbf{u}_{1:k-1}, \mathbf{m})$ at time $k-1$ is essentially the posterior
 221 distribution of \mathbf{x}_{k-1} . The second component $p(\mathbf{y}_k \mid \mathbf{x}_k, \mathbf{m})$ is the measurement
 222 density given the state \mathbf{x}_k and the reference map \mathbf{m} . It is also known as the
 223 likelihood of observing \mathbf{y}_k at state \mathbf{x}_k .

224 The BPF falls into the same Bayesian localisation framework. One of the
 225 major differences is that variables become boxes. This paper uses $[\mathbf{m}]$ to indi-
 226 cate an inaccurate OSM. The evolution and observation models are, therefore,
 227 rewritten as

$$\begin{cases} [\mathbf{x}_k] = [\mathbf{f}]([\mathbf{x}_{k-1}], \mathbf{u}_k) + [\boldsymbol{\mu}_k], \\ [\mathbf{y}_k] = [\mathbf{g}]([\mathbf{x}_k], [\mathbf{m}]) + [\boldsymbol{\nu}_k], \end{cases} \quad (9)$$

228 where $[\mathbf{f}]$ and $[\mathbf{g}]$ are the corresponding inclusion functions.

229 This paper develops a BPF based localisation framework with evolution and
 230 observation models given in (9) within the Bayesian framework.

231 4.2. Bayesian Paradigm of Box Particle Filter for Localisation

232 The BPF employs a set of N weighted boxes $\{(w_k^i, [\mathbf{x}_k^i])\}_{i=1}^N$ to approximate
 233 the point-wise state estimation. For clarity, this paper decomposes the BPF
 234 based localisation into the following four steps.

235 4.2.1. The Predictive Distribution

236 The equivalent prior distribution at time $k-1$ as in (8) is defined as

$$p(\mathbf{x}_{k-1} \mid \mathbf{y}_{1:k-1}, \mathbf{u}_{1:k-1}, [\mathbf{m}]) \approx \sum_{i=1}^N w_{k-1}^i \mathcal{U}_{[\mathbf{x}_{k-1}^i]}(\mathbf{x}_{k-1}), \quad (10)$$

237 where $\mathcal{U}_{[\mathbf{x}]}(\cdot)$ denotes the multivariate uniform probability density function (pdf)
 238 with the interval $[\mathbf{x}]$ as support. The predictive distribution is now given as

$$\begin{aligned} & p(\mathbf{x}_k \mid \mathbf{y}_{1:k-1}, \mathbf{u}_{1:k}, [\mathbf{m}]) \\ & \approx \int p(\mathbf{x}_k \mid \mathbf{x}_{k-1}, \mathbf{u}_k) \sum_{i=1}^N w_{k-1}^i \mathcal{U}_{[\mathbf{x}_{k-1}^i]}(\mathbf{x}_{k-1}) d\mathbf{x}_{k-1} \\ & = \sum_{i=1}^N w_{k-1}^i \int_{[\mathbf{x}_{k-1}^i]} p(\mathbf{x}_k \mid \mathbf{x}_{k-1}, \mathbf{u}_k) \mathcal{U}_{[\mathbf{x}_{k-1}^i]}(\mathbf{x}_{k-1}) d\mathbf{x}_{k-1}, \end{aligned} \quad (11)$$

239 The integral in (11) indicates the distribution of the predicted state after
 240 propagating the i -th box $[\mathbf{x}_{k-1}^i]$ through $[\mathbf{f}]$. This leads to

$$p(\mathbf{x}_k \mid \mathbf{x}_{k-1}, \mathbf{u}_k) \mathcal{U}_{[\mathbf{x}_{k-1}^i]}(\mathbf{x}_{k-1}) = \mathbf{0}, \quad (12)$$

241 $\forall \mathbf{x}_k \notin [\mathbf{f}]([\mathbf{x}_{k-1}^i], \mathbf{u}_k) + [\boldsymbol{\mu}_k]$. This limits the distribution of the predicted state
 242 \mathbf{x}_k to

$$\begin{aligned} & \int_{[\mathbf{x}_{k-1}^i]} p(\mathbf{x}_k \mid \mathbf{x}_{k-1}, \mathbf{u}_k) \mathcal{U}_{[\mathbf{x}_{k-1}^i]}(\mathbf{x}_{k-1}) d\mathbf{x}_{k-1} \\ & \approx \mathcal{U}_{[\mathbf{f}]([\mathbf{x}_{k-1}^i], \mathbf{u}_k) + [\boldsymbol{\mu}_k]}(\mathbf{x}_k) = \mathcal{U}_{[\mathbf{x}_{k|k-1}^i]}(\mathbf{x}_k). \end{aligned} \quad (13)$$

243 By substituting (13) into (11), the predictive distribution becomes

$$p(\mathbf{x}_k \mid \mathbf{y}_{1:k-1}, \mathbf{u}_{1:k}, [\mathbf{m}]) \approx \sum_{i=1}^N w_{k-1}^i \mathcal{U}_{[\mathbf{x}_{k|k-1}^i]}(\mathbf{x}_k). \quad (14)$$

244 4.2.2. The Posterior Distribution

245 The likelihood component $p(\mathbf{y}_k \mid \mathbf{x}_k, [\mathbf{m}])$ is critical in getting the posterior
 246 distribution $p(\mathbf{x}_k \mid \mathbf{y}_{1:k}, \mathbf{u}_{1:k}, [\mathbf{m}])$. In BPF, the likelihood is defined as

$$p(\mathbf{y}_k \mid \mathbf{x}_k, [\mathbf{m}]) = \mathcal{U}_{[\mathbf{y}_k]}(\mathbf{g}(\mathbf{x}_k, [\mathbf{m}])). \quad (15)$$

247 The definition indicates how predicted measurement $\mathbf{g}(\mathbf{x}_k, [\mathbf{m}])$ is distributed
 248 within the support determined by $[\mathbf{y}_k]$, where the observation noise $[\boldsymbol{\nu}_k]$ is con-
 249 sidered.

250 The posterior distribution is now given as

$$\begin{aligned} & p(\mathbf{x}_k \mid \mathbf{y}_{1:k}, \mathbf{u}_{1:k}, [\mathbf{m}]) \\ & = \frac{1}{\chi_k} p(\mathbf{y}_k \mid \mathbf{x}_k, [\mathbf{m}]) p(\mathbf{x}_k \mid \mathbf{y}_{1:k-1}, \mathbf{u}_{1:k}, [\mathbf{m}]) \\ & = \frac{1}{\chi_k} \mathcal{U}_{[\mathbf{y}_k]}(\mathbf{g}(\mathbf{x}_k, [\mathbf{m}])) \sum_{i=1}^N w_{k-1}^i \mathcal{U}_{[\mathbf{x}_{k|k-1}^i]}(\mathbf{x}_k) \\ & = \frac{1}{\chi_k} \sum_{i=1}^N w_{k-1}^i \mathcal{U}_{[\mathbf{x}_{k|k-1}^i]}(\mathbf{x}_k) \mathcal{U}_{[\mathbf{y}_k]}(\mathbf{g}(\mathbf{x}_k, [\mathbf{m}])), \end{aligned} \quad (16)$$

251 in which, the last two terms imply a CSP problem

$$X_k^i \subseteq [\mathbf{x}_k^i] = \{\mathbf{x}_k^i \in [\mathbf{x}_{k|k-1}^i] \mid \mathbf{g}(\mathbf{x}_k^i, [\mathbf{m}]) \in [\mathbf{y}_k]\}, \quad (17)$$

252 i.e. X_k^i is a subset of the predicted state $[\mathbf{x}_{k|k-1}^i]$ that satisfies the measurement
 253 constraint (also refer to (1) for understanding). When a contractor is applied,
 254 the updated state $[\mathbf{x}_k^i]$ that satisfies $X_k^i \subseteq [\mathbf{x}_k^i]$ can be obtained. Hence, the
 255 following relationship holds according to (Gning et al., 2013)

$$\begin{aligned} \mathcal{U}_{[\mathbf{x}_k^i]}(\mathbf{x}_k) &= \mathcal{U}_{[\mathbf{x}_{k|k-1}^i]}(\mathbf{x}_k) \mathcal{U}_{[\mathbf{y}_k]}(\mathbf{g}(\mathbf{x}_k, [\mathbf{m}])) \\ &= \frac{1}{|[\mathbf{x}_{k|k-1}^i]|} |[\mathbf{x}_k^i]| \mathcal{U}_{[\mathbf{x}_k^i]}(\mathbf{x}_k) \frac{1}{|[\mathbf{y}_k]|}, \end{aligned} \quad (18)$$

256 and the posterior distribution in (16) can be simplified as

$$\begin{aligned} &p(\mathbf{x}_k \mid \mathbf{y}_{1:k}, \mathbf{u}_{1:k}, [\mathbf{m}]) \\ &= \frac{1}{\chi_k} \sum_{i=1}^N w_{k-1}^i \frac{1}{|[\mathbf{y}_k]|} \frac{1}{|[\mathbf{x}_{k|k-1}^i]|} |[\mathbf{x}_k^i]| \mathcal{U}_{[\mathbf{x}_k^i]}(\mathbf{x}_k) \\ &\propto \sum_{i=1}^N w_{k-1}^i \frac{|[\mathbf{x}_k^i]|}{|[\mathbf{x}_{k|k-1}^i]|} \mathcal{U}_{[\mathbf{x}_k^i]}(\mathbf{x}_k). \end{aligned} \quad (19)$$

257 4.2.3. Weight Update and Re-sampling

258 In BPF, particle weights are updated via

$$w_k^i \propto w_{k-1}^i * L_k^i, \quad (20)$$

259 with $L_k^i = \frac{|[\mathbf{x}_k^i]|}{|[\mathbf{x}_{k|k-1}^i]|}$, and $0 \leq L_k^i \leq 1$.

260 When relation (17) is absolutely or strongly violated (measurements are not
 261 compatible with the prediction), $|[\mathbf{x}_k^i]|$ becomes zero or negligible. This leads
 262 the updated weight w_k^i to be zero or negligible as well. It will cause the particle
 263 degeneracy phenomenon where only a few particles are with prominent weights.
 264 The re-sampling procedure is then triggered when the following N effective
 265 criterion meets

$$\frac{1}{\sum_i w_k^i} < \eta_{eff} N. \quad (21)$$

266 Re-sampling is done by subdividing boxes of high weights from randomly se-
 267 lected dimensions (Gning et al., 2013), or from the most pessimistic state di-
 268 mensions (the longest box edge corresponded dimension) (Merlinge et al., 2019).

269 *4.2.4. Point State Estimate and Covariance*

270 By nature, interval analysis based methods do not provide point estimates.
 271 To provide statistical metrics such as expectation and covariance, in accordance
 272 with (Merlinge et al., 2019), this paper defines the point expectation as

$$\hat{\mathbf{x}}_k \triangleq \mathbb{E}[\mathbf{x}_k \sim p(\mathbf{x}_k \mid \mathbf{y}_{1:k}, \mathbf{u}_{1:k}, [\mathbf{m}])] \approx \sum_i^N w_k^i \mathbf{c}_k^i, \quad (22)$$

273 which is used as point state estimate at time instant k , with \mathbf{c}_k^i indicates the
 274 center of $[\mathbf{x}_k^i]$, and $\mathbb{E}[\cdot]$ is the statistical expectation.

275 *4.3. Features-refined Box Particle Filter*

276 *4.3.1. Features-refined Contraction*

277 As shown in (1) and (17), contraction accounts for merging innovations into
 278 predicted states to make them accurate and reliable. For a given state $[\mathbf{x}]$
 279 and measurements $\{[\mathbf{y}_i] \in \mathbb{I}\mathbb{R}^d, i = 1, \dots, n\}$ of a feature, there are two ways
 280 to accomplish contraction. The first follows a step-wise paradigm, i.e. doing
 281 contraction upon the arrival of each measurement. The step-wise contraction
 282 is widely accepted and has been applied in (Abdallah et al., 2008) and (Gning
 283 et al., 2013). Alternatively, one can integrate if not all but several measurements
 284 before contraction. It is, therefore, named features-refined contraction in this
 285 paper. **Note** that this paper omits the time stamp k for the purpose of a general
 286 description. This paper also denotes $\{[\mathbf{y}_k^i], i = 1, \dots, n\}$ as $\{[\mathbf{y}_i], i = 1, \dots, n\}$
 287 for brevity.

288 Jaulin (Jaulin, 2009a) has proved that the order of variables being contracted
 289 does not affect the convergent boxes. However, there lacks research works in
 290 literature demonstrating that the features-refined contraction is equivalent to
 291 the step-wise counterpart. The problem will be formulated and their equivalence
 292 will be proved as follows.

293 **Step-wise contraction:** Given a state $[\mathbf{x}]$ and measurements $\{[\mathbf{y}_i] \in \mathbb{I}\mathbb{R}^d, i =$
 294 $1, \dots, n\}$ of a feature, the step-wise contraction result is obtained by solving a

295 CSP problem

$$[s\mathbf{x}_i] = \{s\mathbf{x}_i \in [\mathbf{x}_i] \mid \mathbf{h}(s\mathbf{x}_i) = \mathbf{0}\}, \quad (23)$$

296 where

$$\mathbf{h}(s\mathbf{x}_i) = s\mathbf{x}_i - \mathbf{g}^{-1}([\mathbf{y}_i]), \quad (24)$$

297 $[s\mathbf{x}_{i-1}] = [\mathbf{x}_i]$ holds for $i \in \{2, \dots, n\}$, and $[\mathbf{x}_1] = [\mathbf{x}]$.

298 For localisation, (23) reduces to

$$\begin{aligned} [s\mathbf{x}_n] &= [s\mathbf{x}_{n-1}] \cap \mathbf{g}^{-1}([\mathbf{y}_n]) \\ &= [s\mathbf{x}_{n-2}] \cap \mathbf{g}^{-1}([\mathbf{y}_{n-1}]) \cap \mathbf{g}^{-1}([\mathbf{y}_n]) \\ &\quad \vdots \\ &= [s\mathbf{x}_1] \cap \bigcap_{i=2}^n \mathbf{g}^{-1}([\mathbf{y}_i]) \\ &= [\mathbf{x}] \cap \bigcap_{i=1}^n \mathbf{g}^{-1}([\mathbf{y}_i]), \end{aligned} \quad (25)$$

299 where \mathbf{g}^{-1} is an arbitrary function that is piece-wisely monotonic (Rohou et al.,
300 2018). The final result $[s\mathbf{x}_n]$ can be abbreviated as $[s\mathbf{x}]$ without causing confu-
301 sions.

302 **Features-refined contraction:** Given $[\mathbf{x}]$ and measurements $\{[\mathbf{y}_i] \in \mathbb{I}\mathbb{R}^d, i =$
303 $1, \dots, n\}$ of a feature, the features-refined contraction result $[b\mathbf{x}]$ can be obtained
304 through

$$[b\mathbf{x}] = \{b\mathbf{x} \in [\mathbf{x}] \mid \mathbf{h}(b\mathbf{x}) = \mathbf{0}\}, \quad (26)$$

305 where

$$\mathbf{h}(b\mathbf{x}) = b\mathbf{x} - \mathbf{g}^{-1}\left(\bigcap [\mathbf{y}_i]\right). \quad (27)$$

306 Similarly, for localisation, (26) reduces to

$$[b\mathbf{x}] = [\mathbf{x}] \cap \mathbf{g}^{-1}\left(\bigcap_{i=1}^n [\mathbf{y}_i]\right). \quad (28)$$

307 **Corollary 1:** Given a state $[\mathbf{x}]$ and measurements $\{[\mathbf{y}_i] \in \mathbb{I}\mathbb{R}^d, i = 1, \dots, n\}$
308 of a feature, $[s\mathbf{x}] = [b\mathbf{x}]$ stands, i.e.

$$\bigcap_{i=1}^n \mathbf{g}^{-1}([\mathbf{y}_i]) \cap [\mathbf{x}] = \mathbf{g}^{-1}\left(\bigcap_{i=1}^n [\mathbf{y}_i]\right) \cap [\mathbf{x}]. \quad (29)$$

309 The proof of the corollary is given in [Appendix A](#). When \mathbf{g}^{-1} is nonlinear,
 310 the inclusion function $[\mathbf{g}^{-1}]$ is usually used instead to deal with the contraction
 311 problem. The disadvantage is that it degenerates **Corollary 1** because inclusion
 312 functions usually overly enlarge (or shrink) box volumes. This paper proposes
 313 **Corollary 2** to show results when it comes to inclusion function cases.

314 **Corollary 2:** Given a state $[\mathbf{x}]$ and measurements $\{[\mathbf{y}_i] \in \mathbb{I}\mathbb{R}^d, i = 1, \dots, n\}$,
 315 and a piece-wisely monotonic function \mathbf{g}^{-1} with the corresponding inclusion
 316 function $[\mathbf{g}^{-1}]$, the following equation stands.

$$[\mathbf{g}^{-1}](\bigcap_{i=1}^n [\mathbf{y}_i]) \cap [\mathbf{x}] \subseteq \bigcap_{i=1}^n [\mathbf{g}^{-1}]([\mathbf{y}_i]) \cap [\mathbf{x}]. \quad (30)$$

317 This implies when inclusion functions are used, results from a features-refined
 318 contraction are finer than those from the step-wise contraction, which means
 319 more non-feasible solutions are excluded by the features-refined contraction.

320 The proof of **Corollary 2** is given in [Appendix B](#). Combining **Corollary**
 321 **1** and **Corollary 2**, one can conclude that the features-refined contraction pro-
 322 duces finer results than step-wise contraction despite incorporating the same
 323 measurements. This helps in mitigating the ‘conservative’ aspect of interval
 324 analysis based methods that involve contraction to refine results.

325 **Example 1:** Fig. 1 gives an example where $n = 3$ to show the difference
 326 between the step-wise and features-refined contractions, in scenarios where \mathbf{g}^{-1}
 327 and its inclusion function counterpart $[\mathbf{g}^{-1}]$ are used, respectively. Each step in
 328 Fig. 1 is explained separately as follows.

329 **The first step:** The upper sub-column shows that given three measure-
 330 ments $[\mathbf{y}_1]$, $[\mathbf{y}_2]$, and $[\mathbf{y}_3]$, one can get their intersection $[\mathbf{y}] = \bigcap_{i=1}^3 [\mathbf{y}_i]$ as shown
 331 in the lower sub-column.

332 **The second and third step:** Given \mathbf{g}^{-1} (rather than $[\mathbf{g}^{-1}]$) and $[\mathbf{y}_1]$, $[\mathbf{y}_2]$,
 333 $[\mathbf{y}_3]$, it is intuitive to begin with calculating $\mathbf{g}^{-1}([\mathbf{y}_1])$, $\mathbf{g}^{-1}([\mathbf{y}_2])$, and $\mathbf{g}^{-1}([\mathbf{y}_3])$
 334 for refining $[\mathbf{x}]$ to get $X \in [\mathbf{x}]$. This is usually achieved by following either (25)
 335 or (28). Step 2 shows the step-wise contraction achieved by following (25).
 336 Note that the line width is varied to show that the contraction is done by using
 337 $\mathbf{g}^{-1}([\mathbf{y}_1])$ to $\mathbf{g}^{-1}([\mathbf{y}_3])$ step by step. Step 3, on the other hand, demonstrating

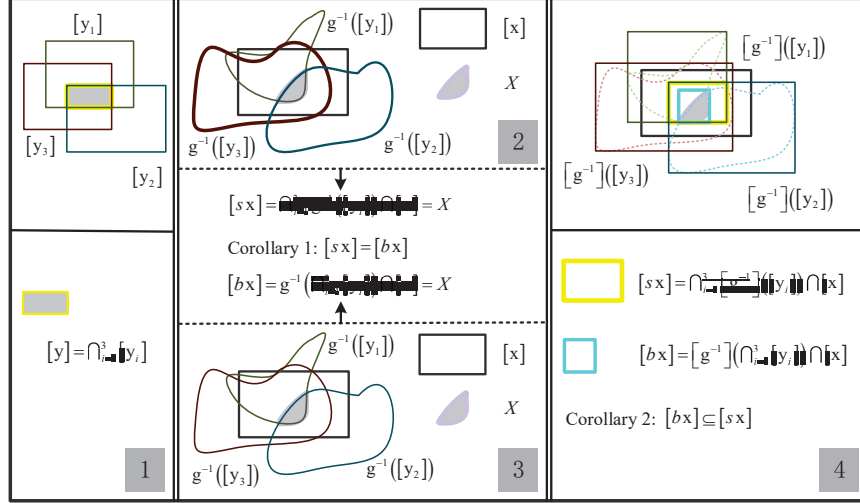


Figure 1: An example illustrating the difference between the step-wise and features-refined contractions. Step 1 gives the intersection of three measurements $[y] = \bigcap_{i=1}^3 [y_i]$. Step 2 and 3 together demonstrate Corollary 1. Note that the line width varies in Step 2 to show the contraction is done step-wisely. Step 4 demonstrates Corollary 2.

338 that $\mathbf{g}^{-1}(\bigcap_{i=1}^3 [y_i])$ is calculated first, which is next used to refine \mathbf{x} to get X .

339 Step 2 and 3 together constitute Corollary 1.

340 Note that when \mathbf{g}^{-1} is used, X is not necessarily a box. It can be of any shape
 341 as shown by the shaded area in the second and third step. The disadvantage is
 342 the computation of X is usually complex. Furthermore, if one gets another \tilde{X}
 343 through other measurements, the calculation of the intersection between X and
 344 \tilde{X} is complex as well.

345 **The fourth step:** To simplify the computation, the inclusion function $[g^{-1}]$
 346 of \mathbf{g}^{-1} is introduced. It converts $\mathbf{g}^{-1}([y_1])$, $\mathbf{g}^{-1}([y_2])$, and $\mathbf{g}^{-1}([y_3])$ into three
 347 boxes denoted by $[g^{-1}([y_1])]$, $[g^{-1}([y_2])]$, and $[g^{-1}([y_3])]$. It is intuitive that
 348 the operation on the latter three boxes is simplified comparing to the operation
 349 on $\mathbf{g}^{-1}([y_1])$, $\mathbf{g}^{-1}([y_2])$, and $\mathbf{g}^{-1}([y_3])$.

350 One can now either follow the step-wise contraction to refine $[x]$ to get $[sx]$,
 351 or use the features-refined contraction to refine $[x]$, resulting in $[bx]$. They

352 are separately shown in Step 4 in Fig. 1, with $[\mathbf{s}\mathbf{x}]$ depicted by the yellow
 353 rectangle and $[\mathbf{b}\mathbf{x}]$ in cyan rectangle in the lower sub-column. One can see that
 354 $[\mathbf{b}\mathbf{x}] \subseteq [\mathbf{s}\mathbf{x}]$ stands. This demonstrates the feature-refined contraction yields
 355 ‘finer’ results compared with step-wise contraction, which would help to mitigate
 356 the ‘conservative’ aspect of interval analysis based methods.

357 In real applications, $\bigcap_{i=1}^n [\mathbf{y}_i]$ could result in an empty intersection despite
 358 a subset with non-empty intersection of the measurements $\{[\mathbf{y}_i] \in \mathbb{I}\mathbb{R}^d, i =$
 359 $1, \dots, n\}$ can still help in contraction. Therefore, (5) is exploited to find a
 360 q -satisfied intersection to approximate $\bigcap_{i=1}^n [\mathbf{y}_i]$. As $q \leq n$ holds, for a given
 361 predicted state $[\mathbf{x}]$, the following equation stands,

$$[q\mathbf{x}] = \{q\mathbf{x} \in [\mathbf{x}] \mid \mathbf{h}(q\mathbf{x}) = \mathbf{0}\}, \quad (31)$$

362 where

$$\mathbf{h}(q\mathbf{x}) = q\mathbf{x} - [\mathbf{g}^{-1}] \left(\bigcap_{j \in A} [\mathbf{y}_j] \right), \quad (32)$$

363 and $[q\mathbf{x}]$ is the result obtained by applying contraction to $[\mathbf{x}]$ with measurement
 364 achieved through q -satisfied intersection. One can directly see the following
 365 condition stands.

$$[\mathbf{g}^{-1}] \left(\bigcap_{i=1}^n [\mathbf{y}_i] \right) \cap [\mathbf{x}] \subseteq [\mathbf{g}^{-1}] \left(\bigcap_{j \in A} [\mathbf{y}_j] \right) \cap [\mathbf{x}], \quad (33)$$

366 where $\bigcap_{j \in A} [\mathbf{y}_j] = \bigcap^{\{q\}} [\mathbf{y}]_{1, \dots, n}$ with $A \subseteq \{1, \dots, n\}$ as defined in (5).

367 4.3.2. Weight Balance

368 In BPF, particle weights are updated through (20), which indicates that
 369 given w_{k-1}^i , the weight w_k^i at time k is proportional to the likelihood L_k^i . One
 370 can generalise (20) by writing

$$w_k^i = w_{k-1}^i * \exp(L_k^i - L_{\max}), \quad (34)$$

371 where $L_{\max} = \max\{L_k^i \mid i = 1, \dots, N\}$, and $\exp(L_k^i - L_{\max})$ is a factor ac-
 372 counting for weight updating. This is because when $0 \leq L_k^i \leq 1$ stands,
 373 $\exp(L_k^i - L_{\max})$ can be approximated by $(L_k^i - L_{\max})$, which still matches the
 374 proportional relationship given by (20).

375 This paper proposes to balance the weight updating formula (34) by

$$w_k^i = w_{k-1}^i * (\exp(L_k^i - L_{\max}) * \alpha + \exp(L_{\text{med}} - L_k^i) * (1 - \alpha)), \quad (35)$$

376 where L_{med} is the median value of $\{L_k^i \mid i = 1, \dots, N\}$, α is the balance param-
377 eter, and $\exp(L_k^i - L_{\max}) * \alpha + \exp(L_{\text{med}} - L_k^i) * (1 - \alpha)$ is the weight updating
378 factor (WUF).

379 By comparing (34) with (35), one can see that the latter keeps $\exp(L_k^i -$
380 $L_{\max})$, meaning that a high likelihood box particle will maintain a high weight
381 after it is updated through (35). Meanwhile, the term $\exp(L_{\text{med}} - L_k^i) * (1 - \alpha)$
382 is added to account for low likelihood box particles that are consistent with the
383 real vehicle state but unlikely due to map errors. This helps also to mitigate the
384 negative effects where the high likelihood is caused by inaccurate OSM features.

385 Fig. 2 shows how WUF changes when α decreases from 1.0 to 0. When one
386 investigates the curves along the left vertical axis, the blue curve is generated
387 by setting $\alpha = 1.0$. The subsequent nine light blue curves from bottom to top
388 are separately generated by setting $\alpha = \{0.9, 0.8, \dots, 0.2, 0.1\}$. The magenta
389 curve is generated by setting $\alpha = 0$. When α is set to 1.0, one can see that (35)
390 becomes equivalent to (34). When it keeps decreasing, WUF tends to balance
391 between high and low likelihood box particles. When α reaches 0, WUF is solely
392 determined by $\exp(L_{\text{med}} - L_k^i)$, which tends to put trust on low likelihood box
393 particles. The values for generating Fig. 2 are $L_{\text{med}} = 0.3$ and $L_{\max} = 1.0$.

394 4.4. OpenStreetMap Accuracy Evaluation

395 4.4.1. Definition of Coordinate Systems

396 Entities on OSM are encoded by geodetic coordinates, i.e. latitude and
397 longitude. This paper chooses the local East, North, and Up (ENU) coord-
398 inate system to achieve localisation, which makes transforming the geodetic
399 coordinates into the local coordinate system necessary. Compared with other
400 Cartesian coordinate systems such as the Earth-Centered, Earth-Fixed (ECEF)
401 coordinate system, the ENU system provides simple 2D planar projections of

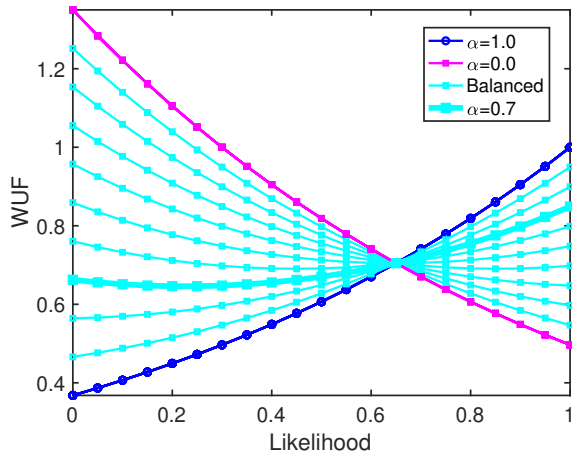


Figure 2: The relationship between likelihood and WUF, with α decreasing from 1.0 to 0. When one focuses on the curves along the left vertical axis, the blue curve is generated by setting $\alpha = 1.0$. The nine light blue curves from bottom to top are separately generated by setting $\alpha = \{0.9, 0.8, \dots, 0.2, 0.1\}$. The curve with $\alpha = 0.7$ is highlighted in bold, which is used in this paper. The magenta curve is generated by setting $\alpha = 0$.

402 geodetic coordinates of interest. Also, the transformation from 3D geodetic co-
 403 ordinates to the ENU coordinate system is invertible, which makes it easy for
 404 transforming localisation results to the geodetic coordinate system if needed.
 405 The transformation between different coordinate systems is shown in Fig. 3.
 406 In this paper, as the campus is roughly flat, the ‘Up’ dimension is omitted for
 407 brevity. Fig. 4 shows how one line feature extracted from LiDAR perception
 408 is represented in the OSM and vehicle coordinate systems. The $O_G-x_Gy_G$ indi-
 409 cates the OSM (and the HDM) coordinate system. The $O_R-x_Ry_R$ is the vehicle
 410 coordinate system. p_j and α_j are separately the distance and angle of the line
 411 feature with respect to $O_G-x_Gy_G$. r_i and ψ_i are the distance and angle of the
 412 line feature with respect to $O_R-x_Ry_R$, respectively.

413 4.4.2. Accuracy Evaluation of OpenStreetMap

414 A customised HDM serves as the local ENU coordinate system in this paper
 415 and the OSM is aligned to it for OSM evaluation, as shown in Fig. 4. Aligning

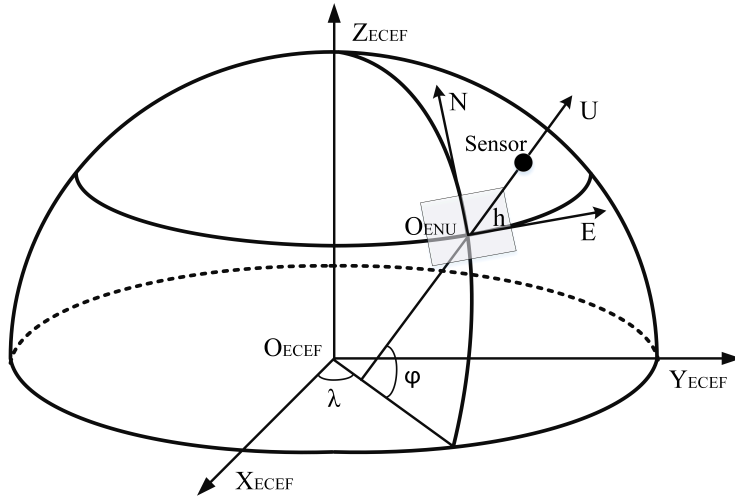


Figure 3: The ENU coordinate system used and the transformation with other systems, λ indicates the longitude, φ indicates the latitude, and h is the ellipsoidal height.

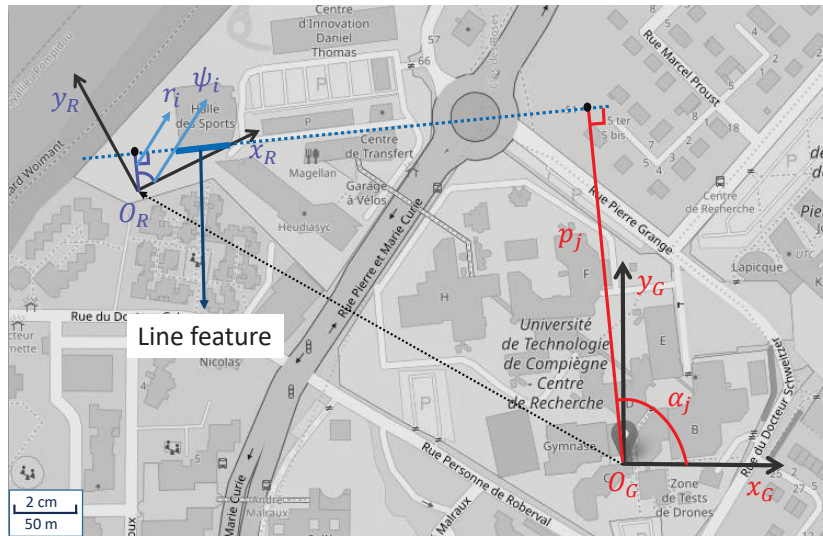


Figure 4: Coordinate systems used for line feature representation.

416 OSM to the HDM coordinate system can lead to negative coordinates of OSM
 417 data, which is caused by projecting geodetic coordinates of OSM into the local
 418 HDM coordinate system. The HDM provides accurate ENU coordinates of
 419 points along the road. There are points along centers of the roads, and points
 420 that mark the boundaries of the roads, as shown in Fig. 5(a). This paper
 421 considers only OSM features within the UTC campus are considered as shown
 422 in Fig. 5(b).

423 This paper adopts the distance from HDM points to the corresponding OSM
 424 roads as a measure of the OSM accuracy. A whole accuracy evaluation of OSM
 425 is out the scope of this paper. Instead, three places that are roughly in the
 426 center of the UTC campus have been chosen for evaluation. These three places
 427 are marked as *Road set 1*, *Road set 2*, and *Road set 3*, which are shown in Fig.
 428 5(a).

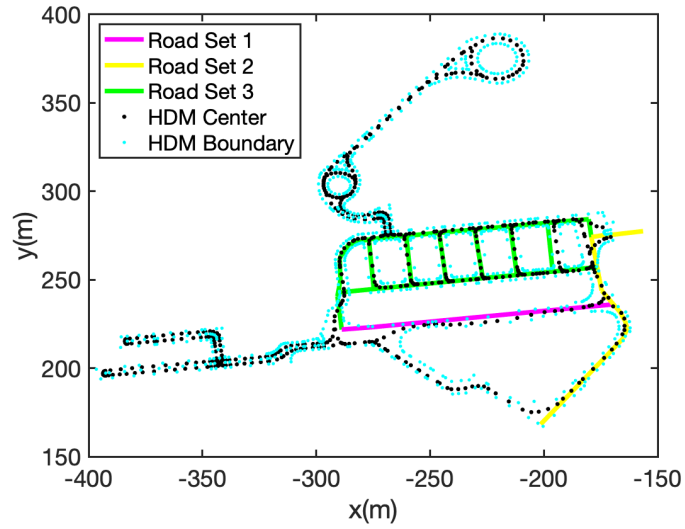
429 A total number of 153 samples from the three places shown in Fig. 5(a) are
 430 used for OSM accuracy evaluation, and the results are summarised in Table I.
 431 It shows that the average distances and the standard deviations from each *Road*
 432 *set*. Column *Road set all* shows results by aggregating distances from all three
 433 places. One can conclude that the OSM accuracy varies even within the UTC
 434 campus. For generality, the results from *Road set all* are taken as evaluation
 435 results. This provides an accuracy of around 0.726 m, with a standard deviation
 436 of 0.778 m.

Table 1: The mean and standard deviation of OSM accuracy evaluation

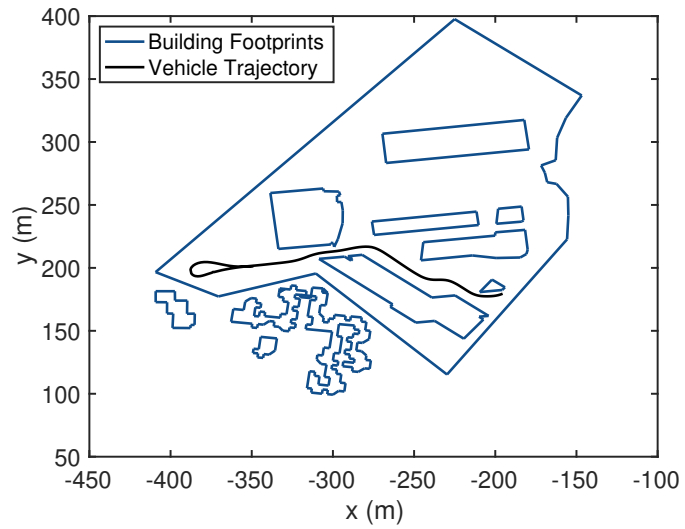
	Road set 1	Road set 2	Road set 3	Road set all
Mean (m)	1.866	0.536	0.556	0.726
Std (m)	1.0870	0.297	0.573	0.778

437 4.5. Measurement and Uncertainty Representation

438 While a vehicle is navigating in an urban environment, various features can
 439 be captured by exteroceptive sensors. This paper only focuses on line features



(a)



(b)

Figure 5: The HDM and building footprints from OSM used for OSM accuracy evaluation. The vehicle trajectory is also given: (a) The HDM and the three sets of data used for OSM accuracy evaluation; (b) The building footprints from OSM of UTC with vehicle trajectory.

440 extracted from LiDAR data, given the fact that they are not only abundant in
 441 structured urban environments but also the fundamental components of OSM.

442 4.5.1. Measurement and Innovation

443 The line feature in Fig. 4 in the $O_G-x_Gy_G$ is represented as

$$x_G \cos \beta_j + y_G \sin \beta_j = p_j, \quad (36)$$

444 where j indicates the line feature is associated with the j -th OSM line feature,
 445 β_j is the angle between the x_G -axis and the line normal vector, and p_j is the
 446 orthogonal distance between O_G and the line.

447 In the vehicle coordinate system $O_R-x_Ry_R$, the line feature is represented as

$$x_R \cos \psi_i + y_R \sin \psi_i = r_i, \quad (37)$$

449 with i marking the i -th line feature in the vehicle coordinate system, ψ_j is the
 450 angle between the O_R -axis and the line normal vector, and r_i is the orthogonal
 451 distance between O_R and the line. Note that (36) and (37) represent the same
 452 line feature in the two different coordinate systems.

453 Distances and angles are taken as feature measurements. By concatenat-
 454 ing the n_R measurements in $O_R-x_Ry_R$ at time k , the measurement vector is
 455 formulated as

$$\mathbf{y}_k = (r_1, \psi_1, r_2, \psi_2, \dots, r_{n_R}, \psi_{n_R})^T. \quad (38)$$

The method proposed in (Teslić et al., 2011) is exploited to associate the
 measurements with OSM features. Without loss of generality, one can assume
 that a feature denoted by (r_i, ψ_i) in $O_R-x_Ry_R$ is associated with a feature de-
 noted by (p_j, β_j) in $O_G-x_Gy_G$. Now, given the predicted vehicle state at time k
 as

$$\mathbf{x}_{k|k-1} = (x_{k|k-1}, y_{k|k-1}, \theta_{k|k-1})^T,$$

456 the feature denoted by (p_j, β_j) in the OSM is transformed into $O_R-x_Ry_R$ by

$$\begin{bmatrix} \tilde{r}_i \\ \tilde{\psi}_i \end{bmatrix} = \begin{bmatrix} |C_j| \\ \beta_j - (\theta_{k|k-1} - \frac{\pi}{2} + (-0.5 \cdot \text{sign}(C_j) + 0.5)\pi) \end{bmatrix}, \quad (39)$$

457 with

$$C_j = p_j - x_{k|k-1} \cos \beta_j - y_{k|k-1} \sin \beta_j. \quad (40)$$

458 By aggregating all the n_R results in (39), the measurement prediction cor-
 459 responding to (38) is denoted as

$$\tilde{\mathbf{y}}_k = (\tilde{r}_1, \tilde{\psi}_1, \tilde{r}_2, \tilde{\psi}_2, \dots, \tilde{r}_{n_R}, \tilde{\psi}_{n_R})^T, \quad (41)$$

460 and the measurement innovation, which is usually defined as the difference be-
 461 tween the measurement in (38) and the measurement prediction given in (41),
 462 is denoted as

$$\mathbf{I}_k = (\Delta r_1, \Delta \psi_1, \Delta r_2, \Delta \psi_2, \dots, \Delta r_{n_R}, \Delta \psi_{n_R})^T, \quad (42)$$

463 with $\Delta r_i = r_i - \tilde{r}_i$, and $\Delta \psi_i = \psi_i - \tilde{\psi}_i$. The innovation \mathbf{I}_k is used to update
 464 the state estimate in filtering techniques such as Kalman filter and particle
 465 filter (Wang et al., 2018).

466 4.6. Measurement and Innovation within Interval Analysis

467 While uncertainties of the line parameters are often taken into account sta-
 468 tistically (Teslić et al., 2011), boxes are used here to represent uncertainties to
 469 the line feature parameters. According to Section 4.4.2, building footprints in
 470 OSMs are shifted (or biased). An interval is added to each endpoint of the line
 471 features in the map to account for the inaccuracy of the OSM. This leads to an
 472 intervalised OSM, which is denoted as $[\mathbf{m}]$.

473 When the OSM is intervalised as $[\mathbf{m}]$, line features in both coordinate sys-
 474 tems are intervalised consequently as

$$[x_G] \cos[\beta_j] + [y_G] \sin[\beta_j] = [p_j], \quad (43)$$

475 and

$$[x_R] \cos[\psi_i] + [y_R] \sin[\psi_i] = [r_i]. \quad (44)$$

476 This equals to adding an box to each measurement (r_i, ψ_i) , turning the mea-
 477 surement in (38) into

$$[\mathbf{y}_k] = ([r_1], [\psi_1], [r_2], [\psi_2], \dots, [r_{n_R}], [\psi_{n_R}])^T, \quad (45)$$

478 and the measurement prediction into

$$[\tilde{\mathbf{y}}_k] = ([\tilde{r}_1], [\tilde{\psi}_1], [\tilde{r}_2], [\tilde{\psi}_2], \dots, [\tilde{r}_{n_R}], [\tilde{\psi}_{n_R}])^T. \quad (46)$$

479 The innovation then becomes

$$[\mathbf{I}_k] = ([\Delta r_1], [\Delta \psi_1], \dots, [\Delta r_{n_R}], [\Delta \psi_{n_R}])^T, \quad (47)$$

480 with $[\Delta r_i] = [r_i] \cap [\tilde{r}_i]$, and $[\Delta \psi_i] = [\psi_i] \cap [\tilde{\psi}_i]$. $[\mathbf{I}_k]$ is used to perform the
 481 contraction. Please note that, as innovations and measurements are directly
 482 related, measurements (and not innovations) are used in formulating and solving
 483 CSPs, in accordance with the literature.

484 4.7. The Features-refined Box Particle Filter based Localisation Algorithm

485 The proposed FRBPF follows a Bayesian approach similar to the BPF de-
 486 scribed in Section 4.2, and the new contraction and weight balance method are
 487 incorporated in FRBPF as Algorithm 1. Fig. 6 gives a graphical representation
 488 of the FRBPF.

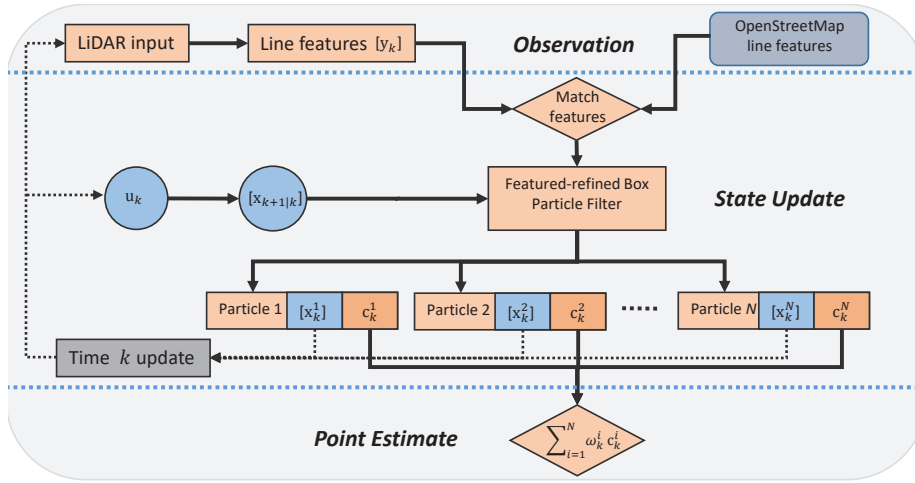


Figure 6: Flowchart of the proposed approach, where k and $k + 1$ are time stamps, $[\mathbf{x}_k^i]$ is the state maintained by the i -th particle, \mathbf{c}_k^i is the center of $[\mathbf{x}_k^i]$, w_k^i is the weight of $[\mathbf{x}_k^i]$, and N is the number of particles.

Algorithm 1 The Features-refined Box Particle Filter

Input: N box particles $\{\mathbf{x}_0^i\}_{i \in \{1, \dots, N\}}$ of empty intersection, whose weights are initiated as $w_0^i = 1/N$, and an OSM $[\mathbf{m}]$.

Output: Point-wise state estimates and box volumes.

- 1: **for** each time-step k **do**
 - 2: Propagate box particles using (9).
 - 3: Calculate innovation using (46, 47).
 - 4: Contract box particles using (31), when an innovation is available.
 - 5: Calculate likelihood and update weights using (35).
 - 6: Weight normalisation.
 - 7: Estimate point state $\hat{\mathbf{x}}_k$ and box volumes.
 - 8: **if** (21) is satisfied **then**
 - 9: Re-sampling: choose a set of particles with the highest weights and determine the new box number n^i per existing box particle.
 - 10: Subdivide each chosen box into n^i new boxes along the most pessimistic dimension and do regularisation by randomly moving the box particles suggested in (Merlinge et al., 2019)
 - 11: Reset all weights to $w_k^i = 1/N$.
-

489 For a line feature from OSM, suppose a set of measurements denoted as
490 $\{[\mathbf{y}_i] \in \mathbb{I}\mathbb{R}^d, i = 1, \dots, n\}$ are obtained. The corresponding predicted measure-
491 ments and innovations are next calculated following equations (46, 47). When
492 the feature-refined contraction and q -satisfied intersection are adopted, (17)
493 becomes (31) to represent the feature-refined contraction problem. As seen ear-
494 lier, the weight updating strategy uses (35) instead of (20), to balance between
495 low and high likelihood box particles to mitigate the localisation uncertainties
496 caused by OSM and measurement uncertainties. Please note that for Step 10,
497 one can either follow the approach in (Merlinge et al., 2019) to subdivide a
498 box along the most pessimistic dimension for re-sampling, or follow the random
499 subdivision approach used in (Abdallah et al., 2008, Gning et al., 2012). Both
500 approaches are studied and their comparison is given in the next section.

501 **5. Performance Evaluation**

502 *5.1. Models and Experiment Settings*

503 The evolution model $[\mathbf{f}]$ uses the measured speed v_k and yaw rate ω_k and is
 504 given as

$$\begin{cases} [x_{k+1}] = [x_k] + T \cdot v_k \cdot \cos([\theta_k] + T \cdot \frac{\omega_k}{2}) + [\mu_k^x], \\ [y_{k+1}] = [y_k] + T \cdot v_k \cdot \sin([\theta_k] + T \cdot \frac{\omega_k}{2}) + [\mu_k^y], \\ [\theta_{k+1}] = [\theta_k] + T \cdot \omega_k + [\mu_k^\theta], \end{cases} \quad (48)$$

505 where $([x_k], [y_k], [\theta_k])^T \triangleq [\mathbf{x}_k]$ is the interval vehicle state, and $([\mu_k^x], [\mu_k^y], [\mu_k^\theta])^T \triangleq$
 506 $[\boldsymbol{\mu}_k]$ is the interval evolution noise.

507 The measurement model $[\mathbf{g}]$ is defined as

$$\begin{cases} [r_k] = \sqrt{([x_k] - [x_R])^2 + ([y_k] - [y_R])^2} + [\nu_k^r], \\ [\psi_k] = \text{atan2}([y_k] - [y_R], [x_k] - [x_R]) - [\theta_k] + [\nu_k^\psi], \end{cases} \quad (49)$$

508 where $[r_k]$ and $[\psi_k]$ are separately the interval distance and angle of a line feature
 509 indicated by $([x_R], [y_R])$ with respect to the vehicle, $([\nu_k^r], [\nu_k^\psi])^T \triangleq [\boldsymbol{\nu}_k]$ is the
 510 interval measurement noise.

511 LiDAR data collected by a Velodyne[®] VLP-16 sensor mounted on the roof of
 512 a vehicle are processed. Sixteen layers of point clouds are obtained. This paper
 513 extracts line segments from these layers directly and they are next associated
 514 with OSM line features. Please note that it is possible that one can extract line
 515 features from point clouds reflected by trees, but they will be filtered out by
 516 data association (no line features corresponding to the tree exist on the OSM)
 517 and q -satisfied intersection (line features corresponding to the same footprint
 518 on the OSM tend to be ‘closer’ to each other than the features from the trees,
 519 hence features extracted from the trees will be filtered out).

520 An abundant number of line segments can be extracted from LiDAR point-
 521 clouds that correspond to a single line feature in OSM. The abundance en-
 522 ables feature-refined contraction and makes the framework proposed meaning-
 523 ful. Ground truth locations are obtained through a RTK sensor suite. Building
 524 footprints of the UTC campus are extracted from [OpenStreetMap](#) as shown in

525 Fig. 5(b). The FRBPF, BRPF, and BPF are implemented in Matlab[®] 2018a
526 programs. The PC configuration includes an Intel[®] Core(TM) i7-7800X CPU
527 and 16.0GB RAM. The box particles do not mutually intersect, and are scat-
528 tered around the initial state of the vehicle provided by the real-time kinematic
529 sensor suite. η_{eff} is set to 0.7 for FRBPF, BRPF, and BPF, which is a common
530 choice (Merlinge et al., 2019). The weight balance parameter α is set to 0.7
531 here. The OSM inaccuracy is incorporated by adding a box $[-0.73 \text{ m}, 0.73 \text{ m}]$
532 (the bounds correspond to the average evaluation error given in Section 4.4)
533 to the distance measurement r , and a box $[-0.5 \text{ rad}, 0.5 \text{ rad}]$ to the angle
534 measurement ψ .

535 5.2. Localisation Performance

536 For general and reliable performance evaluation, $N_{MC} = 100$ times Monte
537 Carlo runs have been carried out for FRBPF, BRPF, and BPF. The point-
538 wise estimation errors and average box volumes are both calculated for per-
539 formance evaluation. The estimation errors are calculated by $RMSE_{\mathcal{X}}(k) =$
540 $\sqrt{\frac{1}{N_{MC}} \sum_{run=1}^{N_{MC}} \|\hat{\mathcal{X}}_{k,run} - \mathcal{X}_{k,run}\|^2}$, with $\hat{\mathcal{X}}_{k,run}$ stands for the estimate at time
541 k and $\mathcal{X}_{k,run}$ is the ground truth. The terms ‘area’ and ‘size’ will be sepa-
542 rately used for position and orientation estimation instead of ‘volume’ to avoid
543 ambiguities. ‘Volume’ will be kept for generic descriptions.

544 Fig. 7 and Fig. 8 show the position and orientation estimation results of
545 FRBPF, BRPF, and BPF, respectively. Both the average box volumes and
546 point-wise estimation errors are given. One can see that FRBPF and BRPF
547 show prominent advantages in terms of both average box volumes and point-
548 wise estimation errors. When compare FRBPF with BRPF, one can see that
549 the former still shows better performance in general, i.e. smaller average box
550 volumes and smaller point-wise estimation errors. It is worth mentioning that
551 there are cases where BRPF slightly outperforms FRBPF. This is due to the
552 reason that when q in q -satisfied intersection is small or around 1, FRBPF
553 degenerates to BRPF, hence leading to similar performance to BRPF.

554

Table 2: Experimental results of FRBPF, BRPF, and BPF. The first two columns are separately the position and orientation errors, and the last two columns are the position box area and orientation box size, respectively.

	Position (m)	Orientation (rad)	Position Area (m ²)	Orientation Size (rad)
FRBPF	0.368	0.010	1.050	0.387
BRPF	0.409	0.012	1.400	0.439
BPF	0.783	0.034	1.781	0.518

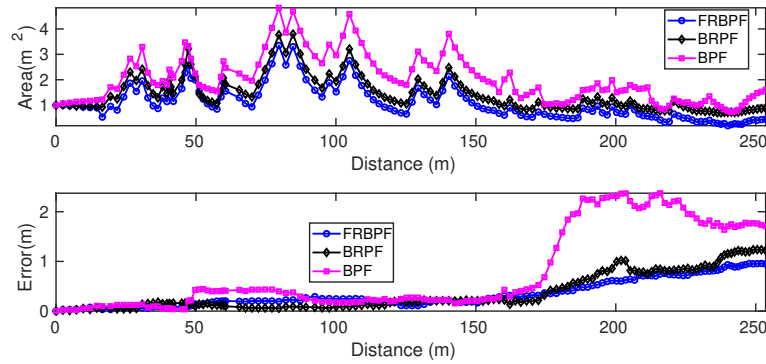


Figure 7: Average position box areas and point-wise position estimation errors.

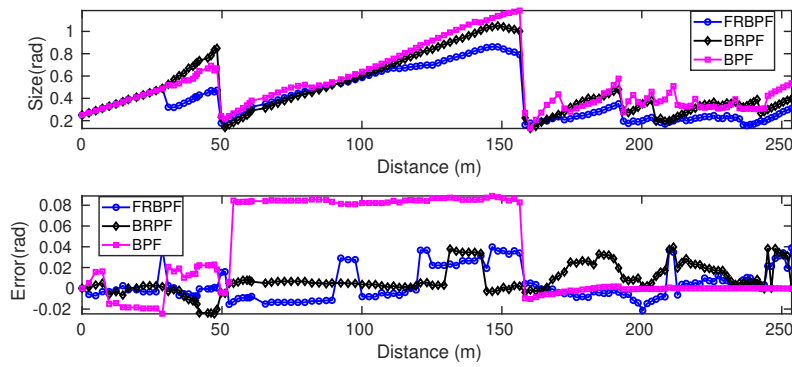


Figure 8: Average orientation box size and point-wise orientation estimation errors.

555 The overall localisation trajectories of FRBPF, BRPF, and BPF are also
556 compared with the ground truth, which is given in Fig. 9. One can see that
557 FRBPF on average achieves the best point-wise localisation results. Fig. 10
558 zooms in the three areas indicated by rectangles to make Fig. 9 easier to read.
559 When compared with BRPF and BPF, FRBPF also performs the best in box
560 volumes reduction. This can be further observed from Table II, which also shows
561 the average point-wise estimation along the full trajectory.

562 The efficiency of FRBPF, BRPF and BPF are at the same level. In par-
563 ticular, FRBPF takes 673 ms in average per step, BRPF takes around 667 ms
564 per step, and BPF takes 647 ms per step on average. FRBPF takes longer
565 partially because of the q -satisfied intersection. This is intuitive as finding the
566 q -satisfied intersection needs extra computational efforts. One can accelerate
567 the q -satisfied intersection by decreasing the box number by a greater step than
568 1. In addition, this paper uses Matlab for FRBPF implementation, which is
569 generally slower than implementations by languages such as C++. It is also
570 worth mentioning that compared with Merlinge et al. (2019), Abdallah et al.
571 (2008), this paper counts time consumed by extracting line features from Li-
572 DAR data and associating them with OSM, etc., which would also contribute
573 to the total execution time.

574 5.3. Discussions

575 5.3.1. Box Area Reduction

576 Figs. 7 and 8 show that the proposed FRBPF has a reduced average box
577 volumes compared with BRPF and BPF. To make it easier to understand, the
578 box hull is adopted as an additional indicator for visualisation and comparison.

579 Fig. 11 shows boxes and the corresponding box hulls from one iteration of
580 FRBPF, BRPF, and BPF, respectively. To be precise, the box-hull area of
581 FRBPF as given in Fig. 11(a) is 43.75 m², which implies an average box area
582 of 0.68 m². In contrast, the box-hull areas of BRPF and BPF are separately
583 46.46 m² and 56.94 m², as shown in Fig. 11(b) and Fig. 11(c). The corresponding
584 average box areas are 0.73 m² and 0.89 m², respectively. One can therefore

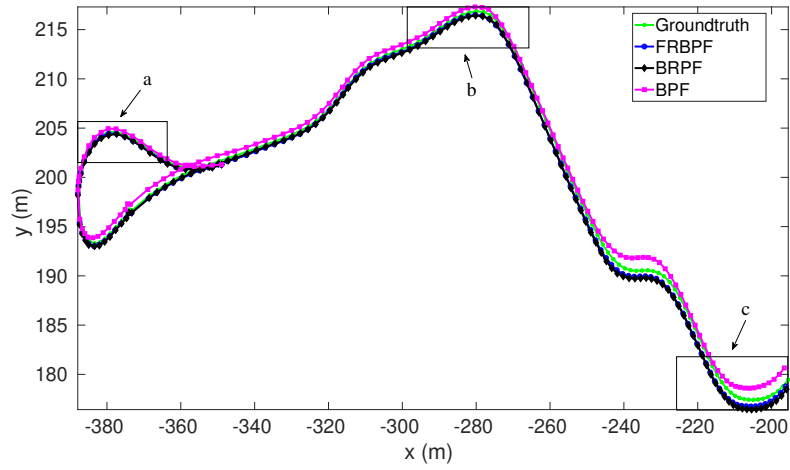


Figure 9: Comparison of FRBPF results with BRPF, BPF, and the ground truth.

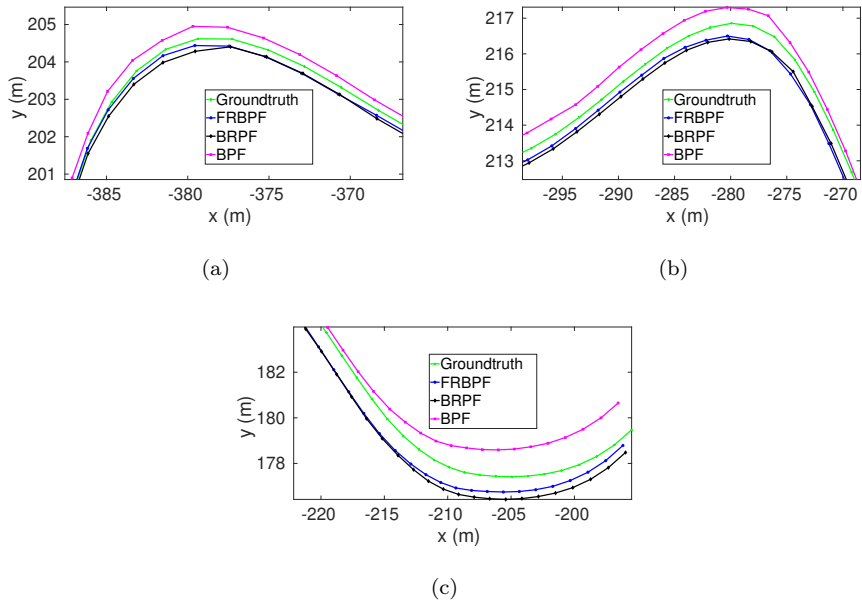


Figure 10: Zoomed figures indicated by rectangles in Fig. 9.

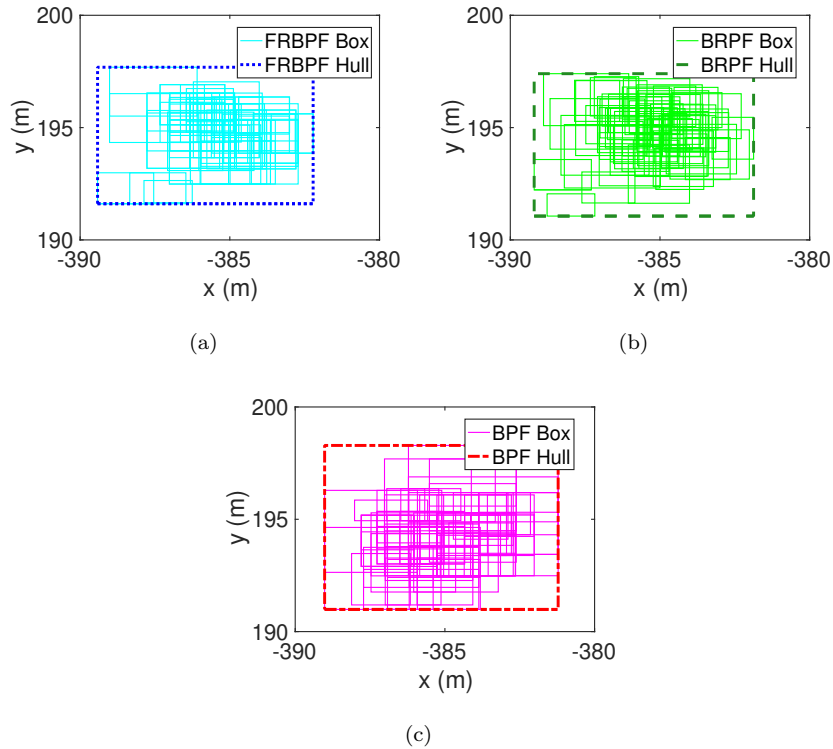


Figure 11: Boxes and box hulls of FRBPF, BRPF, and BPF from one iteration. The dashed rectangles represent box hulls, and rectangles within the box hulls are boxes from each algorithm.

585 conclude that FRBPF helps in box areas reduction, which holds when q in the q -
 586 satisfied intersection equals or slightly smaller than the number of line features.
 587 In the worst case, i.e. $q = 1$ and one randomly selects one measurement for
 588 contraction, it could lead to the increase of the box-hull area. Alternatively, if all
 589 the measurements are used for contraction one by one, then FRBPR degenerates
 590 to BRPF, hence the box-hull area would be similar to BRPF. This can be
 591 observed from Figs. 7 and 8.

592 5.3.2. The Impacts of Weight Balance

593 Let consider the case shown in Fig. 12, where the footprint of a building
 594 on OSM does not align with the real surface due to the inaccuracy of the map-

595 ping. Let's suppose there are only two predicted boxes denoted by $[\mathbf{x}_{k|k-1}^i]$ and
596 $[\mathbf{x}_{k|k-1}^j]$, with areas $||[\mathbf{x}_{k|k-1}^i]||$ and $||[\mathbf{x}_{k|k-1}^j]||$, respectively. Without loss of gener-
597 ality, let's also assume that $||[\mathbf{x}_{k|k-1}^j]|| = ||[\mathbf{x}_{k|k-1}^i]||$ with the same weights. In this
598 example, the vehicle is located within $[\mathbf{x}_{k|k-1}^i]$. When the vehicle gets a LiDAR
599 point cloud reflected by the real surface, a set of measurements $\mathbf{y}_k = ([r_1], [\psi_1])^T$
600 is obtained from the extracted line feature. In the meantime, a corresponding
601 set of predicted measurements can be calculated based on the state prediction
602 and the OSM feature for each particle. The predicted measurements for the
603 two particles in Fig. 12 are denoted as $\tilde{\mathbf{y}}_k^i = ([\tilde{r}_1^i], [\tilde{\psi}_1^i])^T$ and $\tilde{\mathbf{y}}_k^j = ([\tilde{r}_1^j], [\tilde{\psi}_1^j])^T$.
604 Innovations $([\Delta r_1^i], [\Delta \psi_1^i])^T$ and $([\Delta r_1^j], [\Delta \psi_1^j])^T$ are next calculated following
605 (47) for contraction.

606 Without loss of generality, let assume that $[\Delta \psi_1^i] = [\Delta \psi_1^j]$, which makes the
607 contraction solely depending on $[\Delta r_1^i]$ and $[\Delta r_1^j]$. When $||[\Delta r_1^j]|| > ||[\Delta r_1^i]||$, it
608 means that the measurement $([r_1], [\psi_1])^T$ is more compatible with $([\tilde{r}_1^j], [\tilde{\psi}_1^j])^T$
609 than with $([\tilde{r}_1^i], [\tilde{\psi}_1^i])^T$. This leads to higher likelihood for particle $[\mathbf{x}_k^j]$ than
610 for $[\mathbf{x}_k^i]$ according to (20). Given that both $([r_1], [\psi_1])^T$ and OSM are identical
611 to each particle, the only reason lies in the difference of the predicted states.
612 As $||[\mathbf{x}_{k|k-1}^j]||$ is assumed to be equal to $||[\mathbf{x}_{k|k-1}^i]||$, one can image the center of
613 $[\mathbf{x}_{k|k-1}^j]$ is further away from the real surface than $[\mathbf{x}_{k|k-1}^i]$, hence further away
614 from the real location of the vehicle. This contradicts with the likelihood of $[\mathbf{x}_k^j]$
615 is higher than $[\mathbf{x}_k^i]$. Hence, the weight balance is incorporated in the FRBPF to
616 mitigate such problems.

617 The importance of weight balance when an OSM is studied further with four
618 settings of α (0.0, 0.5, 0.7, and 1.0). The estimation errors are given in Fig. 13.
619 One can see that when α is used to balance the weight, the point-wise estimation
620 performance of FRBPF is improved as given in Fig. 13(a) and 13(b). It is worth
621 mentioning that when using the weight balance, one should still emphasise on
622 the high likelihood particles by setting α above 0.5. Indeed, when α is set to
623 be small (such as 0 or 0.5), the estimation errors remain high. Based on these
624 results, the value of $\alpha=0.7$ in the best choice with the used OSM.

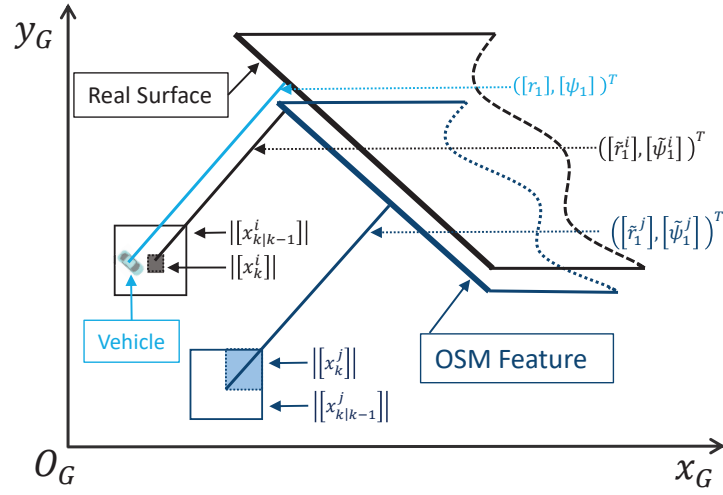


Figure 12: An example demonstrating the necessity of weight balance because of a map error.

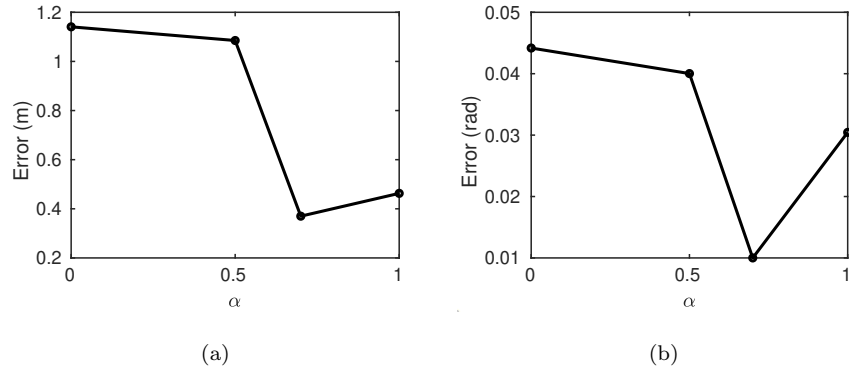


Figure 13: The effect of α on the performance of FRBPF: (a) Average position errors; (b) Average orientation errors.

625 **6. Conclusions**

626 A features-refined box particle filter framework has been proposed. The the-
627 oretical proofs are derived first - about the contraction step which is a key for the
628 reduction of the size of the box particles. Next, the effectiveness of the features-
629 refined box particle filter for vehicle localisation based on OpenStreetMap has
630 been demonstrated. Line features extracted from LiDAR point-clouds are as-
631 sociated with OSM line features to enable features-refined contraction and so
632 improve localisation accuracy. A weight balance strategy has been proposed
633 to improve the performance of the proposed features-refined box particle filter
634 when dealing with the uncertainty present in the map.

635 The proposed framework successfully localises a vehicle using LiDAR and
636 OSM, with better point-wise state estimation accuracy and smaller box volumes
637 compared with the generic box particle filter and the state-of-the-art interval
638 analysis based box regularisation particle filter. The future work will continue
639 in two directions: 1) Fusion of multiple types of sensor data within the box
640 particle filtering approach; 2) Evaluation of the accuracy of OSM in large scale
641 environments, hence focusing on expanding the scalability of the approach.

642 **Appendix A. Proof of Corollary 1**

643 **Proof:** Suppose there exists an x , such that

$$x \in \bigcap_{i=1}^n \mathbf{g}^{-1}([\mathbf{y}_i]).$$

644 which is equivalent to

$$\mathbf{g}(x) \in \bigcap_{i=1}^n [\mathbf{y}_i].$$

645 It can be further rewritten as

$$\mathbf{g}(x) \in [\mathbf{y}_i], \quad i = 1, \dots, n.$$

646 Hence, the following equation holds,

$$x \in \mathbf{g}^{-1}([\mathbf{y}_i]), \quad i = 1, \dots, n,$$

647 which indicates

$$x \in \mathbf{g}^{-1}\left(\bigcap_{i=1}^n [\mathbf{y}_i]\right)$$

648 Therefore, **Corollary 1** is proved.

649 **Appendix B. Proof of Corollary 2**

650 **Proof:** For brevity, let us denote

$$[\mathbf{g}^{-1}]\left(\bigcap_{i=1}^n [\mathbf{y}_i]\right) \triangleq [\mathbf{z}], \quad (\text{B.1})$$

651 where $\mathbf{z} = ([\underline{z}^1, \bar{z}^1], [\underline{z}^2, \bar{z}^2], \dots, [\underline{z}^d, \bar{z}^d])^T$ is a box.

652 According to **Corollary 1**, the following equation holds,

$$\begin{aligned} \mathbf{g}^{-1}\left(\bigcap_{i=1}^n [\mathbf{y}_i]\right) &= \bigcap_{i=1}^n \mathbf{g}^{-1}([\mathbf{y}_i]) \\ &\subseteq [\mathbf{g}^{-1}]\left(\bigcap_{i=1}^n [\mathbf{y}_i]\right). \end{aligned} \quad (\text{B.2})$$

653 In addition, the following equation stands,

$$\bigcap_{i=1}^n \mathbf{g}^{-1}([\mathbf{y}_i]) \subseteq \bigcap_{i=1}^n [\mathbf{g}^{-1}]([\mathbf{y}_i]), \quad (\text{B.3})$$

654 which is in accordance with inclusion function attributes.

655 Now proving **Corollary 2** equals to prove $\forall \mathbf{z}$, if

$$\mathbf{z} \in [\mathbf{g}^{-1}]\left(\bigcap_{i=1}^n [\mathbf{y}_i]\right) \setminus \bigcap_{i=1}^n \mathbf{g}^{-1}([\mathbf{y}_i]) \quad (\text{B.4})$$

656 holds, then the following equation stands,

$$\mathbf{z} \in \bigcap_{i=1}^n [\mathbf{g}^{-1}]([\mathbf{y}_i]). \quad (\text{B.5})$$

657 Suppose that $\exists \mathbf{z}_i = ([\underline{z}_i^1, \bar{x}_i^1], [\underline{x}_i^2, \bar{x}_i^2], \dots, [\underline{x}_i^d, \bar{x}_i^d])^T$ with $i \in \mathbb{N}^+$, equa-
658 tion (B.4) holds but (B.5) does not, which means that there exist at least one
659 dimension $j \in \{1, \dots, d\}$, such that

$$\underline{x}_i^j \geq x_i \quad \text{or} \quad \bar{x}_i^j \leq \bar{x}_i. \quad (\text{B.6})$$

660 Without loss of generality, let's suppose that $\underline{x}_i^j \geq \underline{x}_i$ stands. Then a new box

$$\begin{aligned} \mathbf{o} &= ([\underline{o}_1, \bar{o}_1], [\underline{o}_2, \bar{o}_2], \dots, [\underline{o}_N, \bar{o}_N]) \\ &= \mathbf{x} \setminus \mathbf{x}_i \end{aligned} \tag{B.7}$$

661 can be obtained, which satisfies

$$\mathbf{o} \cap \mathbf{g}^{-1} \left(\bigcap_{i=1}^n [\mathbf{y}_i] \right) \neq \emptyset. \tag{B.8}$$

662 This contradicts (B.3). Therefore, **Corollary 2** stands.

663 **Acknowledgment**

664 Experiments were carried out in the framework of the Equipex ROBOTEX
 665 (ANR-10- EQPX-44-01). We are grateful also to the support by the National
 666 Natural Science Foundation of China (Grant No. 61703387), UK EPSRC for
 667 funding this work through EP/T013265/1 project NSF-EPSRC:ShiRAS - To-
 668 wards Safe and Reliable Autonomy in Sensor Driven Systems and the USA
 669 National Science Foundation under Grant NSF ECCS 1903466.

670 **References**

- 671 Abdallah, F., Gning, A., Bonnifait, P., 2008. Box particle filtering for nonlinear
 672 state estimation using interval analysis. *Automatica* 44 (3), 807–815.
- 673 Alefeld, G., Mayer, G., 2000. Interval analysis: theory and applications. *Journal*
 674 *of Computational and Applied Mathematics* 121 (1-2), 421–464.
- 675 Brovelli, M.A., Minghini, M., Molinari, E.M., Zamboni, G., 2016. Positional
 676 accuracy assessment of the openstreetmap buildings layer through automatic
 677 homologous pairs detection: The method and a case study. *International*
 678 *Archives of the Photogrammetry, Remote Sensing and Spatial Information*
 679 *Sciences* 41, 615–620.

- 680 Drevelle, V., Bonnifait, P., 2013. Localization confidence domains via set inver-
681 sion on short-term trajectory. *IEEE Transactions on Robotics* 29 (5), 1244–
682 1256.
- 683 Freitas, A.D., Mihaylova, L., Gning, A., Schikora, M., Ulmke, M., Angelova, D.,
684 Koch, W., 2018. A box particle filter method for tracking multiple extended
685 objects. *IEEE Transactions on Aerospace and Electronic Systems* 55 (4),
686 1640–1655.
- 687 Gil, A., Juliá, M., Reinoso, Ó., 2015. Occupancy grid based graph-SLAM using
688 the distance transform, SURF features and SGD. *Engineering Applications*
689 *of Artificial Intelligence* 40, 1–10.
- 690 Gning, A., Ristic, B., Mihaylova, L., 2012. Bernoulli particle/box-particle filters
691 for detection and tracking in the presence of triple measurement uncertainty.
692 *IEEE Transactions on Signal Processing* 60 (5), 2138–2151.
- 693 Gning, A., Ristic, B., Mihaylova, L., Abdallah, F., 2013. An introduction to
694 box particle filtering [lecture notes]. *IEEE Signal Processing Magazine* 30 (4),
695 166–171.
- 696 Holý, B., 2018. Registration of lines in 2D LIDAR scans via functions of angles.
697 *Engineering Applications of Artificial Intelligence* 67, 436–442.
- 698 Ilog, S., 1999. Revising hull and box consistency. In: *Proceedings of the Inter-*
699 *national Conference on Logic Programming (ICLP)*, MIT Press, pp. 230–245.
- 700 Jaulin, L., 2009a. A nonlinear set membership approach for the localization and
701 map building of underwater robots. *IEEE Transactions on Robotics* 25 (1),
702 88–98.
- 703 Jaulin, L., 2009b. Robust set-membership state estimation; application to un-
704 derwater robotics. *Automatica* 45 (1), 202–206.
- 705 Jaulin, L., Desrochers, B., 2014. Introduction to the algebra of separators with
706 application to path planning. *Engineering Applications of Artificial Intelli-*
707 *gence* 33, 141–147.

- 708 Jaulin, L., Kieffer, M., Didrit, O., Walter, E., 2001. Interval Analysis. In: Ap-
709 plied Interval Analysis. Springer, pp. 11–43.
- 710 Javanmardi, E., Gu, Y., Javanmardi, M., Kamijo, S., 2019. Autonomous vehicle
711 self-localization based on abstract map and multi-channel lidar in urban area.
712 IATSS research 43 (1), 1–13.
- 713 Joshi, A., James, M.R., 2015. Generation of accurate lane-level maps from
714 coarse prior maps and lidar. IEEE Intelligent Transportation Systems Maga-
715 zine 7 (1), 19–29.
- 716 Kuutti, S., Fallah, S., Katsaros, K., Dianati, M., Mccullough, F., Mouzakitis,
717 A., 2018. A survey of the state-of-the-art localization techniques and their po-
718 tentials for autonomous vehicle applications. IEEE Internet of Things Journal
719 5 (2), 829–846.
- 720 Li, J., Zhao, J., Kang, Y., He, X., Ye, C., Sun, L., 2019. DL-SLAM: Direct
721 2.5 D LiDAR SLAM for autonomous driving. In: Proceedings of the IEEE
722 Intelligent Vehicles Symposium (IV), IEEE, pp. 1205–1210.
- 723 Luo, J., Qin, S., 2018. A fast algorithm of simultaneous localization and mapping
724 for mobile robot based on ball particle filter. IEEE Access 6, 20412–20429.
- 725 Merlinge, N., Dahia, K., Piet-Lahanier, H., Brusey, J., Horri, N., 2019. A box
726 regularized particle filter for state estimation with severely ambiguous and
727 non-linear measurements. Automatica 104, 102–110.
- 728 Pendleton, S.D., Andersen, H., Du, X., Shen, X., Meghjani, M., Eng, Y.H.,
729 Rus, D., Ang, M.H., 2017. Perception, planning, control, and coordination
730 for autonomous vehicles. Machines 5 (1), 6–60.
- 731 Reid, T.G., Houts, S.E., Cammarata, R., Mills, G., Agarwal, S., Vora, A.,
732 Pandey, G., 2019. Localization requirements for autonomous vehicles. arXiv
733 preprint arXiv:1906.01061.

- 734 Rohou, S., Jaulin, L., Mihaylova, L., Le Bars, F., Veres, S.M., 2018. Reliable
735 non-linear state estimation involving time uncertainties. *Automatica* 93, 379–
736 388.
- 737 Senaratne, H., Mobasheri, A., Ali, A.L., Capineri, C., Haklay, M., 2017. A
738 review of volunteered geographic information quality assessment methods.
739 *International Journal of Geographical Information Science* 31 (1), 139–167.
- 740 Suger, B., Burgard, W., 2017. Global outer-urban navigation with open-
741 streetmap. In: *Proceedings of the IEEE International Conference on Robotics*
742 *and Automation (ICRA)*, IEEE, pp. 1417–1422.
- 743 Tamas, L., Goron, L.C., 2014. 3D semantic interpretation for robot perception
744 inside office environments. *Engineering Applications of Artificial Intelligence*
745 32, 76–87.
- 746 Teslić, L., Škrjanc, I., Klančar, G., 2011. EKF-based localization of a wheeled
747 mobile robot in structured environments. *Journal of Intelligent & Robotic*
748 *Systems* 62 (2), 187–203.
- 749 Vargas-Munoz, J.E., Srivastava, S., Tuia, D., Falcão, A.X., 2021. Open-
750 streetmap: Challenges and opportunities in machine learning and remote
751 sensing. *IEEE Geoscience and Remote Sensing Magazine* 9 (1), 184–199.
- 752 Wang, P., Chen, Z., Zhang, Q., Sun, J., 2016. A loop closure improve-
753 ment method of gmapping for low cost and resolution laser scanner. *IFAC-*
754 *PapersOnLine* 49 (12), 168–173.
- 755 Wang, P., Xu, P., Bonnifait, P., Jiang, J., 2018. Box particle filtering for SLAM
756 with bounded errors. In: *Proceedings of the International Conference on Con-*
757 *trol, Automation, Robotics and Vision (ICCARV)*, IEEE, pp. 1032–1038.
- 758 Wang, P., Zhang, Q., Chen, Z., 2015. A grey probability measure set based
759 mobile robot position estimation algorithm. *International Journal of Control,*
760 *Automation and Systems* 13 (4), 978–985.

- 761 Zhang, J., Singh, S., 2014. LOAM: Lidar odometry and mapping in real-time.
762 In: Proceedings of Robotics: Science and Systems Conference (RSS), vol. 2,
763 pp. 109–118.
- 764 Zheng, Y., Izzat, I.H., 2018. Exploring openstreetmap capability for road per-
765 ception. In: Proceedings of the IEEE Intelligent Vehicles Symposium (IV),
766 IEEE, pp. 1438–1443.